China Geology

Behavior of apatite in granitic melts derived from partial melting of muscovite in metasedimentary sources

Li-E Gao[a,*], Ling-sen Zeng[a], Ling-hao Zhao[a, b], Jia-hao Gao[a], Zhen Shang[a]

[a] *Key Laboratory of Deep-Earth Dynamics of Ministry of Natural Resources, Institute of Geology, Chinese Academy of Geological Sciences, Beijing* 100037, *China*
[b] *National Research Center for Geoanalysis, Chinese Academy of Geological Science, Beijing* 100037, *China*

A R T I C L E   I N F O

A B S T R A C T

Fluid-absent and fluid-fluxed melting of muscovite in metasedimentary sources are two types of crustal anatexis to produce the Himalaya Cenozoic leucogranites. Apatite grains separated from melts derived from the two types of parting melting have different geochemical compositions. The leucogranites derived from fluid-fluxed melting have relict apatite grains and magmatic crystallized apatite grains, by contrast, there are only crystallized apatite grains in the leucogranites derived from fluid-absent melting. Moreover, apatite grains crystallized from fluid-fluxed melting of muscovite contain higher Sr, but lower Th and LREE than those from fluid-absent melting of muscovite, which could be controlled by the distribution of partitioning coefficient ($D_{Ap/Melt}$) between apatite and leucogranite. $D_{Ap/Melt}$ in granites derived from fluid-absent melting is higher than those from fluid-fluxed melting. So, not only SiO_2 and A/CNK, but also types of crustal anatexis are sensitive to trace element partition coefficients for apatite. In addition, due to being not susceptible to alteration, apatite has a high potential to yield information about petrogenetic processes that are invisible at the whole-rock scale and thus is a useful tool as a petrogenetic indicator.

©2021 China Geology Editorial Office.

1. Introduction

Apatite, a calcium phosphate mineral in common sense, is prevalent in magmatic, metamorphic, and sedimentary rocks (Hughes JM and Rakovan JF, 2015; Henrichs IA et al., 2018; Kirkland CL et al., 2018). Recent advances in the understanding of trace element concentrations, isotope ratios, and U-Pb dating of apatite have demonstrated that apatite provides a potentially robust record for unraveling the provenance of sedimentary rocks (Morton A and Yaxley G, 2007; Gillespie J et al., 2018), metamorphic grade and the protolith of metamorphic rocks (Henrichs IA et al., 2018), magmatic petrogenesis (Bruand E et al., 2014; Kirkland CL et al., 2018; Jiang XY et al., 2018), and the composition of the Hadean (>4 Ga) continental crust (Patrick B et al., 2018; Emo RB et al., 2018).

The formula of apatite can be simplified as $A_5(XO_4)_3Z$. The A-site usually accommodates Ca, but can be substituted by a variety of trace elements including Mn^{2+}, Sr^{2+}, U^{4+}, Pb^{2+}, Th^{4+}, Y^{3+} and $REE^{2+, 3+}$. The tetrahedral X-site is occupied mainly by P^{5+} and can be replaced by other small, highly-charged cations (e.g. Si^{4+}, S^{6+}, As^{5+}, V^{5+}). The monovalent anion Z-site is occupied by OH^- or halogens F^- and Cl^- (Piccoli PM and Candela PA, 2002). Therefore, it can incorporate a large range of elements (such as REE, Sr, Y, Mn, Th, Eu, Nd), which are sensitive to the composition of the host magma and the nature of melt evolution (Bruand E et al., 2014). Apatite derived from different rock types has distinctive absolute and relative abundances of many trace elements, therefore, apatite can be an excellent indicator in understanding the petrogenetic process of granites (Belousova EA et al., 2002; Chu MF et al., 2009; Miles AJ et al., 2014). Moreover, apatite is a mineral able to highlight magmatic events, which are not always visible using whole rock compositions (Bruand E et al. 2014) that have been overprinted by metamorphic processes (Bruand E et al., 2017) or lost from the geological record (Miles AL et al., 2013). These recent advances highlight exciting new horizons to understand igneous processes using apatite.

During crustal partial melting, apatite saturation levels are a function of temperature and composition of the melt (Harrison TM and Watson EB, 1984; Pichavant M et al.,

1992; Wolf MB and London D, 1995; Zeng LS et al., 2005a). In muscovite/biotite dehydration, relict apatite dissolution plays a significant role. In contrast, monazite dissolution is favored during muscovite/biotite fluid-fluxed melting reactions (Zeng LS et al., 2005b; Villaros A et al., 2009; Gao LE et al., 2017; Zeng LS and Gao LE, 2017). Thus, whether apatite crystallized from the two types of crustal partial melting also shows different geochemical characteristics is still an open question. In addition, how the composition of melt controls the elemental concentration in apatite is another important issue. Answers to these questions are crucial to apply apatite as a useful petrogenetic indicator. In this contribution, the authors present trace element composition data in apatite grains from representative leucogranites derived from different partial melting of muscovite. With these data, the authors will discuss the geochemical behavior of apatite in detail and further suggest that apatite could be served as a potential tool to estimate the original magma composition and to reconstruct crustal melting processes.

2. Geological setting

The Himalayan orogen has been considered to result from continental collision between India and Eurasia plates at Cenozoic (Hodges KV, 2000; Yin A and Harrison TM, 2000; Chen J et al., 2010; Dupont-Nivet G et al., 2010; Liebke U et al., 2010). From north to south, there are four lithotectonic domains, Tethyan Himalaya, High Himalaya, Lesser Himalaya, and Sub-Himalaya, which are separated by three major fault zones, Southern Tibet Detachment System (STDS), Main Central Thrust (MCT), and Main Boundary Thrust (MBT) (Fig. 1a). Leucogranites in the Himalayan orogen are mainly distributed along two sub-parallel belts, Tethyan Himalaya and High Himalaya. The Tethyan Himalaya, also named Northern Himalayan Gneiss Domes (NHGD), consists of a series of semi-continuous oval shape gneiss domes which consist of high grade metamorphic rocks and intruded Cenozoic granites (46–8 Ma) in the core and low grade metamorphic or unmetamorphosed sedimentary toward the margin (Zhang HF et al., 2004; Aoya M et al., 2005; Lee J and Whitehouse MJ, 2007; Aikman AB et al., 2008; Zeng LS et al., 2011; King J et al., 2011; Hou ZQ et al., 2012; Gao LE et al., 2014; Liu ZC et al., 2014). In the High Himalaya unit, Cenozoic granites (37–10 Ma) intruded into the High Himalayan Crystalline Sequence (HHCS) (Harrison TM et al., 1999; Murphy MA and Harrison TM, 1999; Searle MP and Godin L, 2003; Cottle JM et al., 2009; Kali E et al., 2010; Leloup PH et al., 2010; Streule M et al., 2010; Yu JJ et al., 2011; Aikman AB et al., 2012). STDS is a large ductile shear zone with a width of > 10 km and a length of 2000 km along the Himalayan orogen and mainly consists of mylonitic gneisses and intruded Cenozoic foliated leucogranites (Yang XY et al., 2009).

The study area, between Yarlung Tsangpo suture (YTS) and MCT, encompasses the Malashan Dome, STDS, and High Himalayan Crystalline Sequence (HHCS) with North-South Trending Rift Zone (NSTR) vertically cutting across

them (Fig 1b; Gao LE et al., 2017). The Malashan Dome consists of Cuobu two-mica granite, Malashan two-mica granite, and Paiku leucogranite in the core and pelitic and calcareous schist toward the margin (Fig. 1b) which experienced relatively intensive contact metamorphism induced by emplacement of granitic plutons. The Paiku composite leucogranite pluton consists of 28.2 Ma tourmaline-bearing leucogranite, 19.8 Ma two-mica granite, and garnet-bearing leucogranite (Gao LE et al., 2013). The Cuobu two-mica granite formed at 26.0–13.7 Ma (Aoya M et al., 2005) and the Malashan two-mica granite at 17.6–16.9 Ma (Aoya M et al., 2005; Gao LE and Zeng LS, 2014), respectively. Within the STDS, strongly foliated 21–20 Ma leucogranites intruded into mylonitized Paleozoic granitic gneisses (Gao LE et al., 2019). In the High Himalaya, 16.0–22.0 Ma undeformed leucogranites as dikes, veins and lenses, intruded into the HHCS (Gao LE et al., 2016). The geochemical nature and the formation mechanism of these leucogranites indicate that there are two types of partial melting in metasedimentary sources: Fluid-absent and fluid-fluxed melting of muscovite (Gao LE et al., 2017). The authors separated apatite grains from representative leucogranites to discuss the differences in the behavior of apatite during different partial melting of muscovite. The leucogranites TMLS, T0646, and T0658 are derived from fluid-fluxed melting of muscovite, whereas T0659-B, T0651, and T0655 are from fluid-absent melting of muscovite (Gao LE et al., 2017). The two types of leucogranites are characterized by similar mineral assemblages and consist of quartz, plagioclase, K-feldspar, muscovite with minor biotite and accessory phases of zircon, apatite, and monazite (Figs. 2, 3).

3. Analytical methods

Trace element analyses of apatite were conducted synchronously by LA-ICP-MS at the State Key Laboratory of Geological Processes and Mineral Resources, China University of Geosciences, Beijing. Detailed operating conditions for the laser ablation system and the ICP-MS instrument and data reduction are followed the procedures described by Gao S et al., (2002) and Liu XM et al. (2002). The NIST 612 apatite was used as a reference standard (Pearce NJG et al., 1997). Spot sizes were 30 μm, the standard apatite was analyzed first and repeated after every ten unknowns. The analytical data are summarized in supplementary Table 1s.

4. Data and results

Apatite grains separated from the two types of leucogranites share similar features. A majority of apatite grains are columnar or granular and are characterized by homogeneous texture (Fig. 3). However, trace element compositions show that there are two types of apatite grains, magmatic and relict apatite grains, in the leucogranites
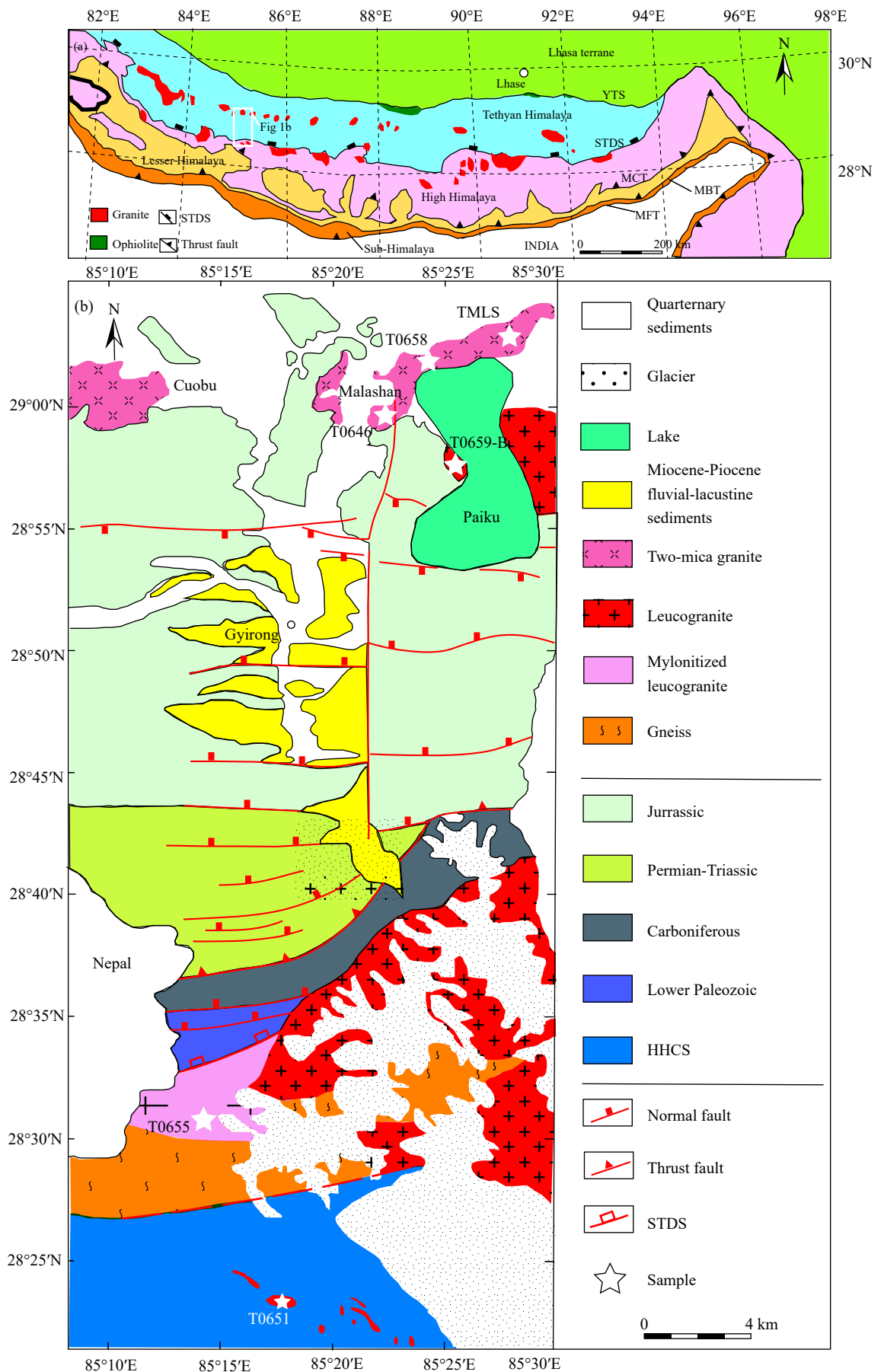
Fig. 1. Simplified geological map of the Himalayan orogenic belt showing the locations of samples. YTS−Yarlung Tsangpo Suture Zone; STDS−southern Tibet Detachment System; MCT−main central thrust; MBT−main boundary thrust; MFT−main frontal thrust.

derived from fluid-fluxed melting of muscovite, whereas there are only magmatic crystallized apatite grains in the leucogranites derived from fluid-absent melting of muscovite (Figs. 4, 5).

Fig. 2. Field photographs of the leucogranites. a, b–leucogranites T0646 and T0658 derived from fluid-fluxed melting of muscovite; and c, d–leucogranites T0655 and T0659-B derived from fluid-absent melting of muscovite.
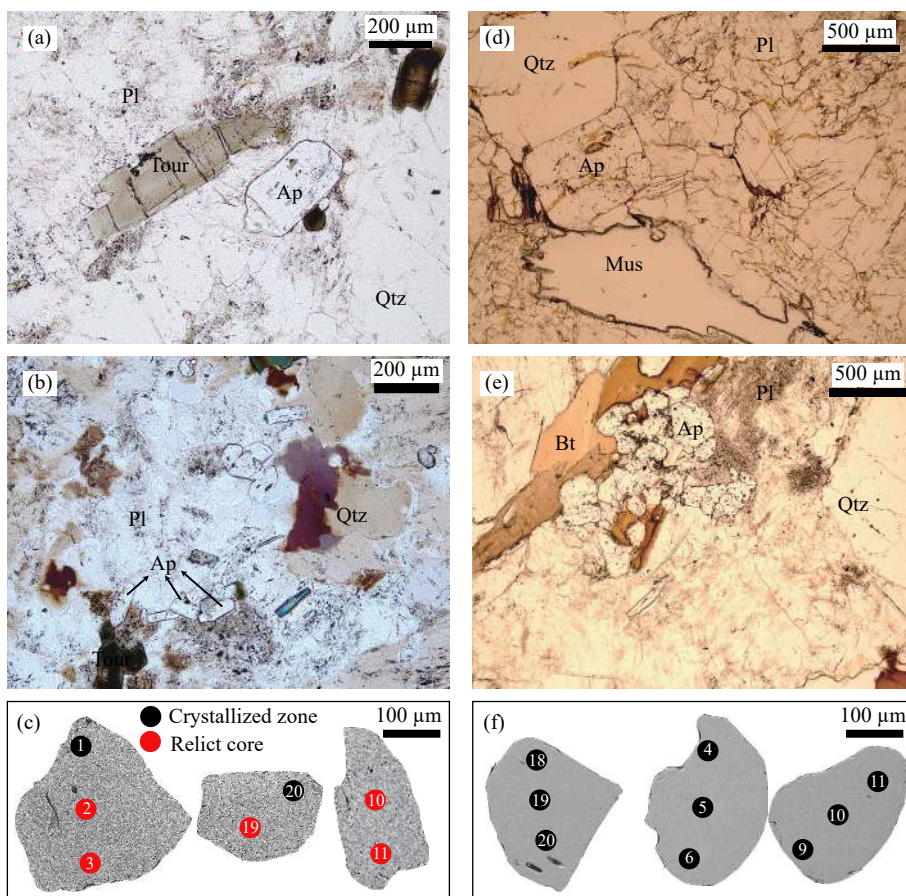

Fig. 3. Photomicrographs of the leucogranites and BSE image of apatite, a–c–from the leucogranites derived from fluid-fluxed melting of muscovite, and d–f– from the leucogranites derived from fluid-absent melting of muscovite in metasedimentary sources. Ap–apatite; Bt–biotite; Mus–muscovite; Pl–plagioclase; Qtz–quartz; Tour–tourmaline.

Magmatic apatite grains are characterized by (1) concaved down REE distribution patterns with $(La/Yb)_N=0.61–1.90$ (Fig. 4); (2) relative to LREE and HREE, slightly enriched in MREE with $(La/Gd)_N=0.30–0.79$ and $(Gd/Yb)_N=1.13–4.32$, (3) pronounced negative Eu anomalies with $Eu/Eu*=0.05–$ 0.30 (Fig. 5d), (4) slightly positive Ce anomalies with $Ce/Ce*=1.00–1.18$ (Fig. 5d), (5) negative Nd anomalies with $Nd/Nd*=0.66–0.91$ ($Nd/Nd* =Nd_N/[(Pr_N^2 \times Sm_N)^{1/3}$, Table 1), (6) positive correlation between Y and Yb (Fig. 5a), and Sr and $Eu/Eu*$ (Fig. 5b), but negative correlation between Sr and

Table 1. Distribution of partitioning coefficient ($D_{Ap/Melt}$) between apatite and leucogranite.

Sample	T0646	T0658	TMLS-09	T0659-B	T0655	T0651
Whole-rock major element (%) and trace element geochemistry ($\times 10^{-6}$)						
SiO_2	71.84	72.81	71.67	73.7	72.36	70.57
Sc	6.46	4.21	4.79	1.67	3.06	10.2
V	29.2	17.3	19.05	3.50	1.73	47.7
Cr	22.6	161	40.5	34.5	2.09	49.8
Ni	8.67	77.2	18.04	16.79	0.6	21.4
Co	3.97	3.6	3.16	1.15	0.82	8.95
Cu	6.11	12.3	6.58	3.45	3.72	8.45
Zn	54.8	48.1	50.15	24.43	46.9	14.1
Ga	22.8	19.5	20.05	22.10	27.1	17.1
Rb	228	205	203	336	385	186
Sr	193	162	180	70.0	60.8	41.2
Y	12.6	12.2	15.55	11.09	11.8	37.5
Zr	76.9	74.8	67.8	30.10	55.8	465
Nb	7.81	5.91	5.78	8.19	7.19	12.50
Sn	3.75	3.89	3.22	11.10	14.1	5.52
Cs	12.1	12	8.665	7.37	40.4	12.4
Ba	557	468	524.5	165	239	194
La	27.8	19.4	24	7.81	13.2	33.8
Ce	57.7	40.4	50.5	16.5	27.8	71.4
Pr	6.35	4.54	5.66	1.88	3.27	7.91
Nd	23.9	16.6	21.05	6.77	11.7	29.50
Sm	5.09	3.81	4.48	1.97	3.47	6.29
Eu	1.05	1.02	1.045	0.38	0.52	1.26
Gd	4.32	3.27	4.115	2.13	3.39	6.74
Tb	0.55	0.46	0.565	0.35	0.51	1.10
Dy	2.76	2.47	2.995	2.05	2.62	6.78
Ho	0.46	0.43	0.54	0.37	0.42	1.37
Er	1.27	1.25	1.52	1.02	1.05	4.12
Tm	0.17	0.17	0.195	0.15	0.13	0.57
Yb	1.15	1.17	1.31	1.02	0.77	3.78
Lu	0.17	0.18	0.18	0.14	0.1	0.56
Hf	2.7	2.75	2.32	1.65	2.43	12.90
Ta	0.79	0.83	0.685	1.99	0.7	1.06
W	0.46	1.34	0.675	1.61	1.81	0.86
Tl	1.05	0.96	0.9	1.40	1.86	0.77
Pb	48	45.1	45.05	47.13	58.8	14.70
Bi	1.33	1.07	0.68	0.12	7.77	0.14
Th	14.2	9.86	12.7	4.40	9.36	22.20
U	1.72	1.77	1.895	1.68	6.87	3.30
A/CNK	1.1	1.18	1.12	1.11	1.05	0.95
Nd/Nd*	0.92	0.88	0.91	0.81	0.80	0.92
Eu/Eu*	0.69	0.89	0.75	0.58	0.47	0.60
LREE	121.89	85.77	106.74	35.31	59.96	150.16
Th	14.20	9.86	12.70	4.40	9.36	22.2
Sr	193.00	162.00	180.00	70.00	60.80	41.2
Ba	557.00	468.00	524.50	164.67	239.00	194
Trace element geochemistry for apatite ($\times 10^{-6}$)						
La	97.45	130.85	125.77	204.71	183.16	244.33
Ce	359.04	444.47	414.81	725.60	600.80	831.31

Table 1 (*Continued*)

Sample	T0646	T0658	TMLS-09	T0659-B	T0655	T0651
Pr	59.40	71.41	67.98	115.28	94.37	136.12
Nd	304.65	357.91	336.17	527.69	430.72	642.14
Sm	144.75	171.44	161.80	298.30	228.10	246.83
Eu	7.17	9.07	9.70	7.91	8.37	14.04
Gd	198.27	233.87	217.08	375.82	310.77	315.49
Tb	40.11	46.97	44.81	75.72	64.92	65.31
Dy	233.72	269.94	265.85	398.56	362.10	411.31
Ho	42.06	47.76	47.94	62.52	60.88	80.88
Er	100.07	111.02	115.57	140.20	138.74	206.67
Tm	12.98	13.81	14.82	18.57	17.12	27.81
Yb	79.78	80.79	87.31	113.46	98.23	174.41
Lu	9.47	9.33	10.29	12.67	11.43	22.48
Sr	128.16	136.70	135.06	66.02	72.24	84.84
Th	1.06	1.34	2.05	3.80	2.26	3.47
Y	1105.04	1230.14	1225.76	1701.27	1648.42	2062.67
Nd/Nd*	0.87	0.85	0.84	0.76	0.77	0.88
Eu/Eu*	0.13	0.14	0.16	0.07	0.10	0.16
$\sum$LREE	972.46	1185.15	1116.23	1879.48	1545.53	2114.75
Th	1.06	1.34	2.05	3.80	2.26	3.47
Sr	128.16	136.70	135.06	66.02	72.24	84.84
Ba	0.26	0.33	0.33	0.30	0.21	0.36
Distribution of partitioning coefficient ($D_{Ap/Melt}$) between apatite and leucogranite						
La	3.51	6.74	5.24	26.20	13.88	7.23
Ce	6.22	11.00	8.21	43.98	21.61	11.64
Pr	9.35	15.73	12.01	61.21	28.86	17.21
Nd	12.75	21.56	15.97	77.98	36.81	21.77
Sm	28.44	45.00	36.12	151.68	65.74	39.24
Eu	6.83	8.89	9.29	20.63	16.10	11.14
Gd	45.90	71.52	52.75	176.44	91.67	46.81
Tb	72.93	102.10	79.32	218.43	127.28	59.38
Dy	84.68	109.29	88.77	194.73	138.20	60.67
Ho	91.44	111.06	88.78	167.46	144.96	59.03
Er	78.80	88.81	76.03	137.01	132.14	50.16
Tm	76.38	81.25	75.98	121.12	131.67	48.79
Yb	69.37	69.05	66.65	111.60	127.58	46.14
Lu	55.71	51.84	57.19	90.48	114.35	40.14
LREE	7.98	13.82	10.46	53.22	25.78	12.52
Th	0.07	0.14	0.16	0.87	0.24	0.16
Sr	0.66	0.84	0.75	0.94	1.19	2.07
Y	87.70	100.83	78.83	153.36	139.70	55.00

Y (Fig. 5c). Compared with magmatic apatite grains, relict apatite grains have relatively higher and more variable Eu anomalies with Eu/Eu*=0.43–1.32 (Fig. 5d), slightly positive Ce anomalies with Ce/Ce*=0.99–1.14 (Fig. 5d), and slightly negative Nd anomalies with Nd/Nd*=0.78–0.96 (Table 1). There are no correlations between Y and Yb, Sr and Eu/Eu*, as well as Sr and Y in relict apatite grains (Fig. 5).

Magmatic apatite grains from leucogranites derived from the two types of partial melting have different geochemical nature. Apatite grains crystallized from fluid-fluxed melting of muscovite have higher Sr (128×10^{-6}–137×10^{-6}), but lower Th (1.06×10^{-6}–2.05×10^{-6}) and LREE (972.5×10^{-6}–1116.2×10^{-6}) than those from fluid-absent melting of muscovite ($Sr<90\times10^{-6}$, $Th >2.26\times10^{-6}$, LREE $>1545.5\times10^{-6}$; Fig. 6).

5. Discussion

Apatite is not susceptible to alteration and is a useful tool for identifying the adakite-like plutons that no longer preserve the initial Sr/Y ratios in whole rocks due to weathering and hydrothermal alteration (Pan LC et al., 2016). Apatite chemistry from granitoids is also extremely powerful for recovering information about the whole rock of their original host and yield information about petrogenetic processes that are invisible at the whole-rock scale (mixing, *in situ* crystal fractionation, metasomatism; Bruand E et al., 2017). A global compilation of granitoids whole rock and apatite chemistry demonstrate a strong correlation between Sr_{Ap} and Sr_{WR} and Sr_{Ap} correlates with SiO_2 in granites (Bruand E et al., 2017). In Fig. 6, it compares Sr, Th, and LREE in apatite grains and

granites. Sample T0651 plots away from the correlation defined by global compilation of whole rock and apatite chemistry in granitoids (Bruand E et al., 2017), which suggests that T0651 has been altered. The Sr composition of granite T0651 has decreased but Th and LREE have increased. Fractional crystallization of plagioclase rich in anorthite component could strongly influence the chemical compositions of the residual melts (Zeng LS et al., 2011). Such a process commonly occurs in magma differentiation in granitic magmas and generally increases the contents of Si, Na, and LREE, but decreases Sr concentrations in the residual

magma (Zeng LS et al., 2012). In primitive mantle-normalized spider diagram and chondrite-normalized REE distribution pattern (Fig. 7), REE, Y, Th, Zr, Hf and Nb also increased in granite T0651 (Table 1). Therefore, it can be interpreted such features as mentioned above in sample T0651 are due to fractional crystallization of plagioclase. The compositions of apatite grains in sample T0651 had not been altered and are identical to other samples derived from fluid-absent melting (Fig. 6; Table 1). Therefore, it infers that Sr of bulk-rock in T0651 should be $80×10^{-6}$, Th=$5.5×10^{-6}$, and $\sum$LREE=$18×10^{-6}$.
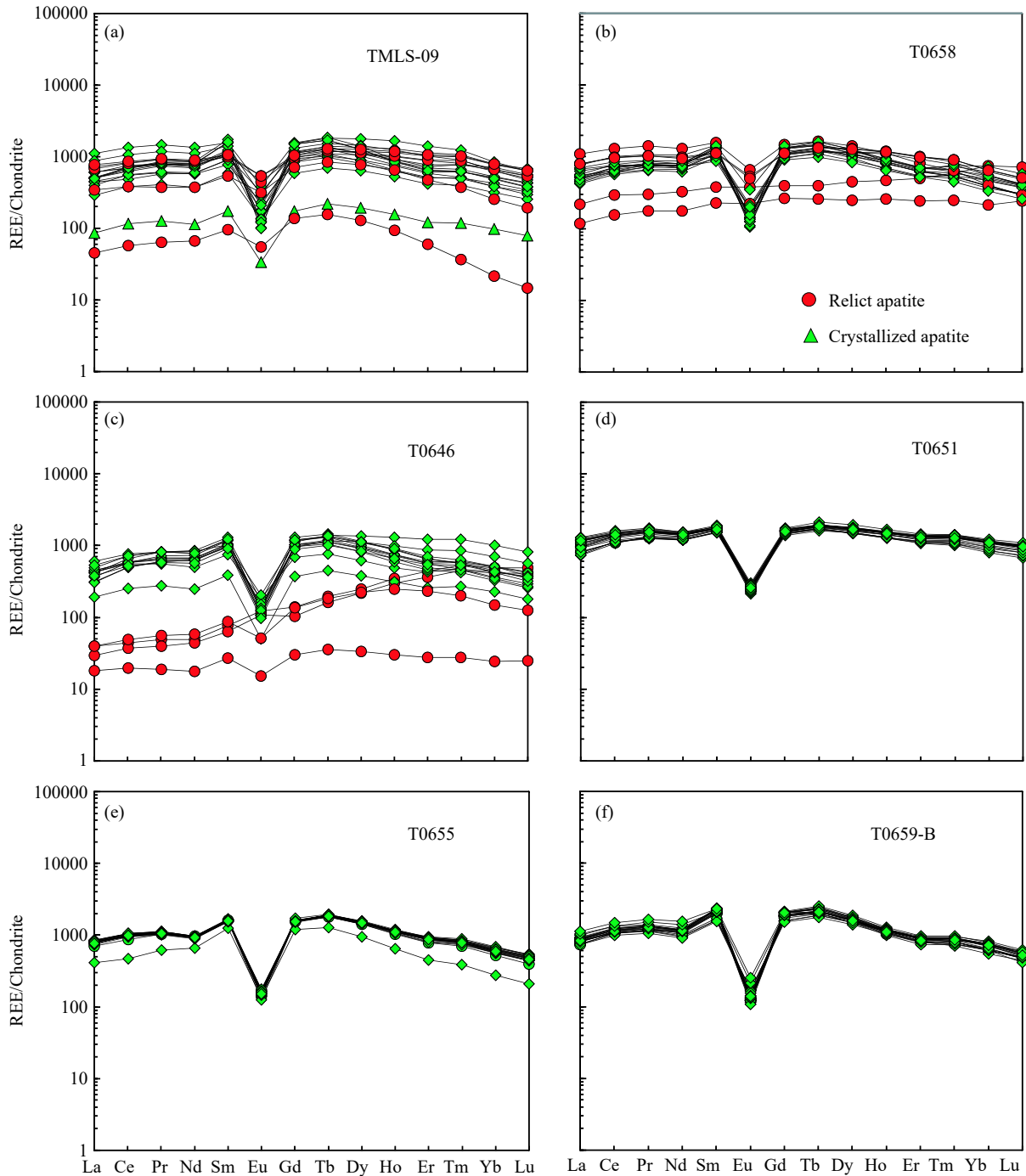
Fig. 4. Chondrite-normalized rare earth element distribution patterns for apatite from leucogranite. Chondrite normalization values are from Sun SS and McDonough WF (1989). a–c–are from the leucogranites derived from fluid-fluxed melting of muscovite, and d–f–from the leucogranites derived from fluid-absent melting of muscovite.
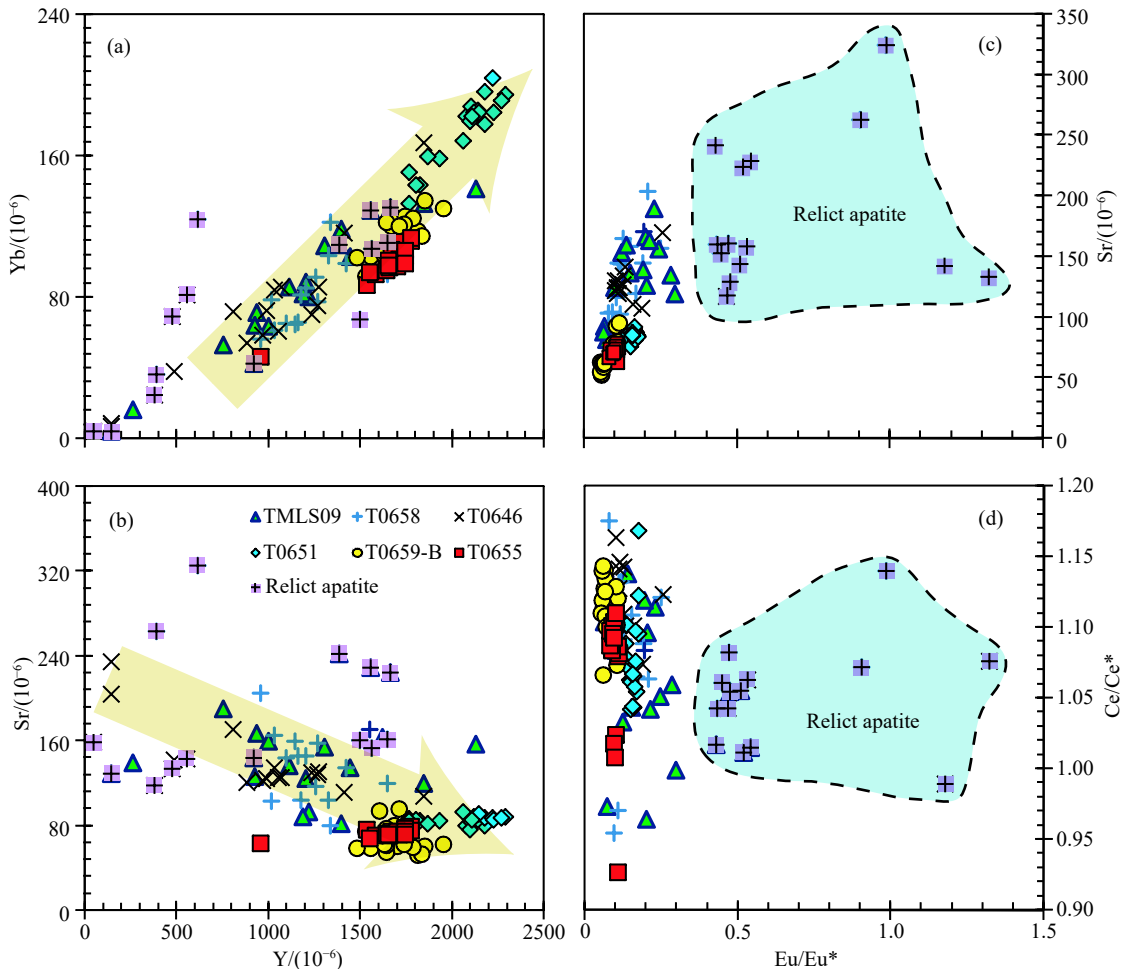
Fig. 5. Trace elements characteristics of apatite from leucogranite.
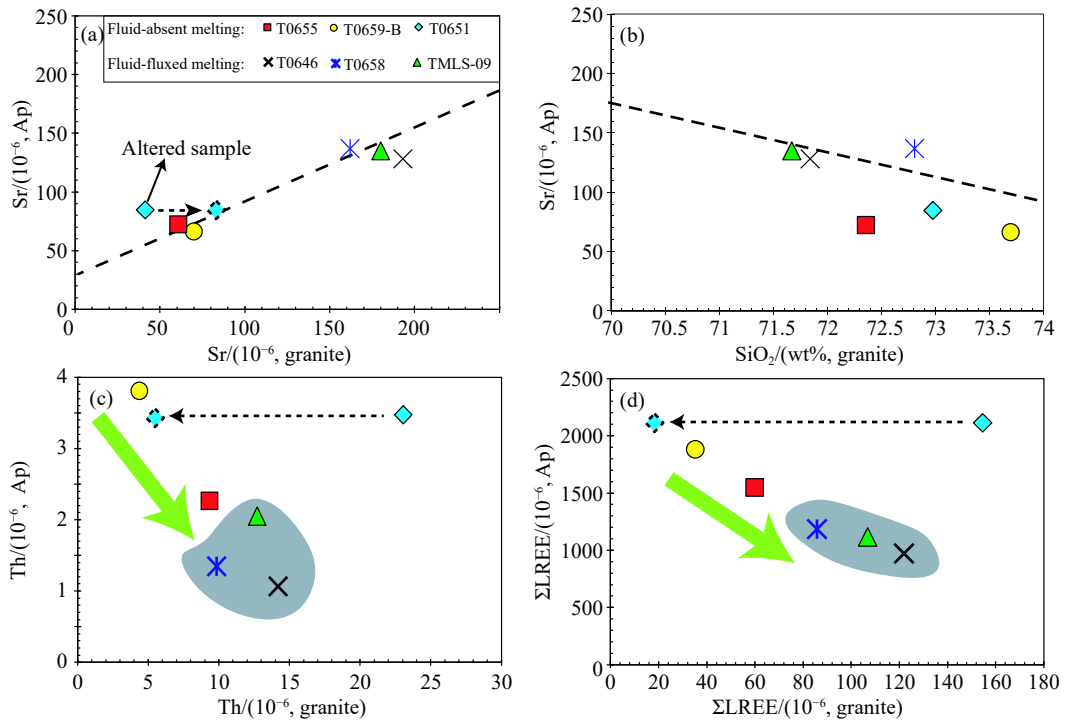
Fig. 6. Average Sr, Th and LREE relationship in apatite and leucogranite. The dotted lines (a, b) represent the correlation defined by global compilation of whole rock and apatite chemistry in granitoids (Bruand E et al., 2017). T0651 plots away from the correlation, which suggests that T0651 has been altered. Sr has decreased and Th and LREE have increased. Sr=80×10⁻⁶, Th=5.5 ×10⁻⁶ and ∑LREE=18×10⁻⁶. The variation of chemical compositions in T0651 is reasonable given the fractional crystallization of plagioclase rich in anorthite component.
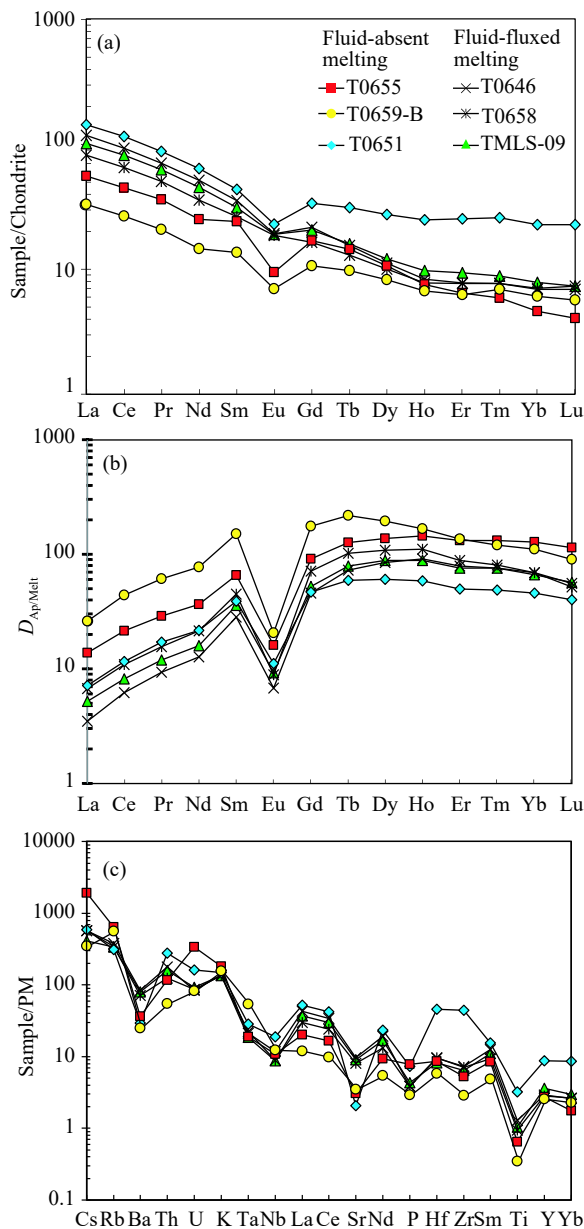
Fig. 7. Chondrite-normalized rare earth element distribution patterns (a) and PM-normalized trace element spider diagrams (c) for leucogranite and distribution of partitioning coefficient ($D_{Ap/Melt}$) of REE between apatite and leucogranite (b). Primitive mantle and chondrite normalization values are from Sun SS and McDonough WF (1989).

Apatite grains during the two types of partial melting of muscovite have different behavior. Gao LE et al., (2017) compared geochemical signatures of fluid-absent versus fluid-fluxed melting of muscovite in metasedimentary sources. The leucogranites derived from fluid-fluxed melting have relatively higher concentrations of Ca, Sr, Ba, Zr, Hf, Th, and LREE, and ratios of Zr/Hf, Eu/Eu*, and Nd/Nd*, but lower Rb, Nb, Ta, and U concentrations, Rb/Sr and $^{87}Sr/^{86}Sr$ ratios, and $\varepsilon_{Hf}(t)$ than the other type of granites. The geochemical differences can be explained by the melting behaviors of major (muscovite, feldspar) and accessory minerals (zircon and monazite) during different modes of crustal anatexis.

Experimental results and theoretical treatments (Harrison TM and Watson EB, 1984; Watson EB and Harrison TM, 1984; Rapp RP and Watson EB, 1986; Pichavant M et al., 1992; Montel JM, 1993; Zeng LS et al., 2005a) have shown that monazite dissolution overwhelms the dissolution of apatite under wet and low-temperature conditions. In contrast, dry and high-temperature conditions favor apatite dissolution. Such inferences are consistent with the observations that leucogranites derived from fluid-fluxed melting of muscovite contain not only magmatic apatite grains but also relict ones (Figs. 3, 4, 5). Owing to the possible low solubility of accessory apatite in granites derived from fluid-fluxed melting of muscovite, trace element contents of relict crystals do not reflect equilibrium with the melt compositions and thus are resemble their parental hosts.

Moreover, apatite grains crystallized from melts from the two types of partial melting have different geochemical characteristics. Different from the bulk compositions of granites, apatite grains crystallized from fluid-fluxed melting of muscovite have lower Th and LREE than those from fluid-absent melting of muscovite (Fig. 6; Table 1), which should be controlled by partitioning coefficient ($D_{Ap/Melt}$) between apatite and leucogranite. Apatite solubility in granitic melts is strongly affected by temperature with minor effects from pressure or dissolved H_2O content (Watson EB and Harrison TM, 1984). Recent experimental work has better characterized trace element partition coefficients for apatite, which are sensitive to changes in magma compositions (e.g., SiO_2 and the aluminum saturation index value; Harrison TM and Watson EB, 1984; Pichavant M et al., 1992). In Fig. 8, although there are different trends in the two types of magmatic apatite grains from fluid-fluxed melting and fluid-absent melting, $D_{Ap/Melt}$ is positively correlated with SiO_2 and A/CNK of granites. Overall, $D_{Ap/Melt}$ in granites derived from fluid-absent melting is higher than those from fluid-fluxed melting (Figs. 7b, 8). The calculated $D_{Ap/Melt}$ in this paper is similar to the partitioning coefficient of REE between apatite and melt (Zeng LS et al., 2012). Therefore, they should represent equilibrium values, and variations in D as shown above are largely due to compositional effect (melt structure) produced by different partial melting reactions. In Fig. 8, although the bulk composition of sample T0651 has been altered, it can be infered partitioning coefficient $D_{Ap/Melt}$ according to SiO_2, $D_{Ap/Melt}$ (La)=20 and $D_{Ap/Melt}$ (Gd)=130, further infer A/CNK (=1.08) in T0651, which suggest that T0651 is peraluminous granite. Therefore, trace element partition coefficients for apatite are sensitive to changes in types of crustal anatexis.

6. Conclusion

There are pronounced differences in the concentrations of the trace elements in apatite grains from melts derived from fluid-fluxed melting versus fluid-absent melting of muscovite in metasedimentary sources. The relict apatite grains are only preserved in melts derived from fluid-fluxed melting reaction.
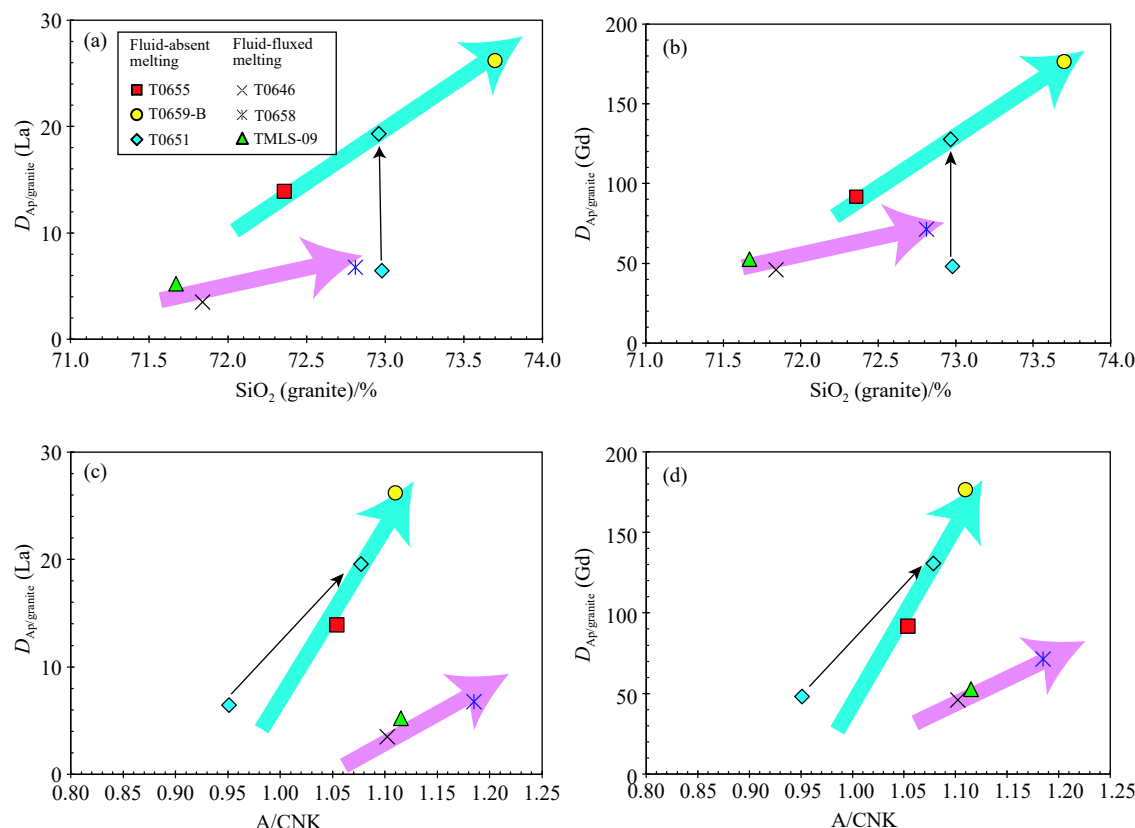
Fig. 8. Distribution of partitioning coefficient ($D_{Ap/Melt}$) between apatite and leucogranite are sensitive to SiO_2, the aluminum saturation index value A/CNK, as well as type of crustal anatexis in leucogranitic magmas.

Apatite grains crystallized from melts derived from fluid-fluxed melting of muscovite contain lower Th and LREE than those from fluid-absent melting of muscovite, which can be attributed to the differences in the partitioning coefficient between apatite and leucogranite: $D_{Ap/Melt}$ in granites derived from fluid-absent melting is higher than those from fluid-fluxed melting. Therefore, trace element partition coefficients for apatite in granitic magmas are sensitive not only to SiO_2 and A/CNK, but also to the types of crustal anatexis. Apatite could be a useful tool to recast the original magma compositions and to recognize crustal melting processes.

CRediT authorship contribution statement

Li-E Gao and Ling-sen Zeng conceived of the presented idea. Ling-hao Zhao, Jia-hao Gao and Zhen Shang carried out the experiment. All authors discussed the results and contributed to the final manuscript.

Declaration of competing interest

The authors declare no conflicts of interest.

Acknowledgment

Supplementary dataset

References

Aikman AB, Harrison TM, Hermann J. 2012. Age and thermal history of Eo- and Neohimalayan granitoids, eastern Himalaya. Journal of Asian Earth Sciences, 51, 85–97. doi: 10.1016/j.jseaes.2012.01.011.

Aikman AB, Harrison TM, Ding L. 2008. Evidence for early (> 44 Ma) Himalayan crustal thickening, Tethyan Himalaya, southeastern Tibet. Earth and Planetary Science Letters, 274, 14–23. doi: 10.1016/j.epsl.2008.06.038.

Aoya M, Wallis SR, Terada K, Lee J, Kawakami T, Wang Y, Heizler M. 2005. North–south extension in the Tibetan crust triggered by granite emplacement. Geology, 33, 853–856. doi: 10.1130/G21806.1.

Belousova EA, Griffin WL, O'Reilly SY, Fisher NI. 2002. Apatite as an indicator mineral for mineral exploration: Trace-element compositions and their relationship to host rock type. Journal of Geochemical Exploration, 76(1), 45–69. doi: 10.1016/S0375-6742(02)00204-2.

Bruand E, Storey C, Fowler M. 2014. Accessory mineral chemistry of high Ba-Sr granites from northern scotland: Constraints on petrogenesis and records of whole-rock signature. Journal of Petrology, 55(8), 1619–1651. doi: 10.1093/petrology/egu037.

Bruand E, Fowler M, Storey C, Darling J. 2017. Apatite trace element

and isotope applications to petrogenesis and provenance. American Mineralogist, 102, 75–84. doi: 10.2138/am-2017-5744.

Chen J, Huang B, Sun L. 2010. New constraints to the onset of the India-Asia collision: Paleomagnetic reconnaissance on the Linzizong Group in the Lhasa Block, China. Tectonophysics, 489, 189–209. doi: 10.1016/j.tecto.2010.04.024.

Chu MF, Wang KL, Griffin WL, Chung SL, O'Reilly SY, Pearson NJ, Iizuka Y. 2009. Apatite composition: Tracing petrogenetic processes in transhimalayan granitoids. Journal of Petrology, 50, 1829–1855. doi: 10.1093/petrology/egp054.

Cottle JM, Searle MP, Horstwood MSA, Matthew SA, Waters David J. 2009. Timing of mid-crustal metamorphism, melting, and deformation in the Mount Everest region of southern Tibet revealed by U (‐Th)‐Pb geochronology. The Journal of Geology, 117(6), 643–664. doi: 10.1086/605994.

Dupont-Nivet G, Lippert PC, van Hinsbergen DJJ, Meijers MJM, Kapp P. 2010. Paleolatitude and age of the Indo- Asia collision: Paleomagnetic constraints. Geophysical Journal International, 182, 1189–1198. doi: 10.1111/j.1365-246X.2010.04697.x.

Emo RB, Smit MA, Melanie S, Ellen K, Scherer EE, Peter S, Bleeker W, Mezger K. 2018. Evidence for evolved hadean crust from sr isotopes in apatite within eoarchean zircon from the acasta gneiss complex. Geochimica et Cosmochimica Acta, S0016703718303089-. doi: 10.1016/j.gca.2018.05.028.

Gao LE, Zeng LS, Hu GY, Wang YY, Wang Q, Guo CL, Hou KJ. 2019. Early Paleozoic magmatismalong the northernmargin of East Gondwana. Lithos, 334 –335, 25–41. doi: 10.1016/j.lithos.2019.03.007.

Gao LE, Zeng LS, Asimow PD. 2017. Contrasting geochemical signatures of fluid-absent versus fluid-fluxed melting of muscovite in metasedimentary sources: The Himalayan leucogranites. Geology, 45(1), 39–42. doi: 10.1130/G38336.1.

Gao LE, Zeng LS, Wang L, Hou KJ, Gao JH, Shang Z. 2016. Timing and tectonic implication of different crustal partial melting in the Himalayan Orogenic Belt. Acta Geologica Sinica, 90(11), 3039–3059 (in Chinese with English abstract).

Gao LE, Zeng LS. 2014. Fluxed melting of metapelite and the formation of Miocene high-CaO two-mica granites in the Malashan gneiss. Geochimica et Cosmochimica Acta, 130, 136–155. doi: 10.1016/j.gca.2014.01.003.

Gao LE, Zeng LS, Hou KJ, Guo CL, Tang SH, Xie KJ, Hu GY, Wang L. 2013. Episodic crustal anatexis and the formation of Paiku composite leucogranitic pluton in the Malashan Gneiss Dome, Southern Tibet. Chinese Science Bulletin, 58, 3546–3563. doi: 10.1007/s11434-013-5792-4.

Gao S, Liu XM, Yuan HL. 2002. Analysis of forty-two major and trace elements of USGS and NIST SRM Glasses by LA-ICPMS. Geostandards Newsletters, 26, 181–196. doi: 10.1111/j.1751-908X.2002.tb00886.x.

Gillespie J, Glorie S, Khudoley A, Collins AS. 2018. Detrital apatite u-pb and trace element analysis as a provenance tool: Insights from the yenisey ridge (siberia). Lithos, 314 –315, 140–155. doi: 10.1016/j.lithos.2018.05.026.

Harrison TM, Watson EB. 1984. The behavior of apatite during crustal anatexis: Equilibrium and kinetic considerations. Geochimica et Cosmochimica Acta, 48, 1467–1478. doi: 10.1016/0016-7037(84)90403-4.

Harrison TM, Grove M, Kevin D, McKeegan KD, Coath CD, Lovera OM, Le Fort P. 1999. Origin and episodic emplacement of the Manaslu intrusive complex, Central Himalaya. Journal of Petrology, 40, 3–19. doi: 10.1093/petroj/40.1.3.

Henrichs IA, O'Sullivan G, Chew DM, Mark C, Babechuk MG, McKenna C, Emo R. 2018. The trace element and U-Pb systematics of metamorphic apatite. Chemical Geology, 483, 218–238. doi: 10.1016/j.chemgeo.2017.12.031.

Hodges KV. 2000. Tectonics of the Himalaya and southern Tibet from two perspectives. Geological Society of America Bulletin, 112, 324–350. doi: 10.1130/0016-7606(2000)1122.3.CO;2.

Hou ZQ, Zheng YC, Zeng LS, Gao LE, Huang KX, Li W, Li QY, Fu Q, Liang W, Sun QZ. 2012. Eocene −Oligocene granitoids in southern Tibet: Constraints on crustal anatexis and tectonic evolution of the Himalayan orogen. Earth and Planetary Science Letters, 349 –350, 38–52. doi: 10.1016/j.epsl.2012.06.030.

Hughes JM, Rakovan, JF. 2015. Structurally robust, chemically diverse: Apatite and apatite supergroup minerals. Elements, 11, 165–170. doi: 10.2113/gselements.11.3.165.

Jiang XY, Li H, Ding X, Wu K, Guo J Liu JQ, Sun WD. 2018. Formation of a-type granites in the lower yangtze river belt: A perspective from apatite geochemistry. Lithos, 304 –307, 125–134. doi: 10.1016/j.lithos.2018.02.005.

Kali E, Leloup P, Arnaud N, Maheo G, Liu D, Boutonnet E, Van der Woerd J, Liu X, L IH. 2010. Exhumation history of the deepest central Himalayan rocks, Ama Drime range: Kwy pressure-temperature-deformation-time constraints on orogenic models. Tectonics, 29(2), TC2014. doi: 10.1029/2009TC002551.

King J, Harris N, Argles T, Parrish R, Zhang HF. 2011. The contribution of crustal anatexis to the tectonic evolution of Indian crust beneath southern Tibet. Geological Society of America Bulletin, 123, 218–239. doi: 10.1130/B30085.1.

Kirkland CL, Yakymchuk C, Szilas K, Evans N, Hollis J, McDonald B, Gardiner NJ. 2018. Apatite: A U-Pb thermochronometer or geochronometer? Lithos, 318 –319, 143–157. doi: 10.1016/j.lithos.2018.08.007.

Lee J, Whitehouse MJ. 2007. Onset of mid-crustal extensional flow in southern Tibet: Evidence from U/Pb zircon ages. Geology, 35, 45–48. doi: 10.1130/G22842A.1.

Leloup PH, Maheo G, Arnaud N, Kali, E, Boutonnet E, Liu XH, Li HB. 2010. The South Tibet detachment shear zone in the Dinggye area: Time constraints on exhumation models of the Himalayas. Earth and Planetary Science Letters, 292(1−20), 1–16. doi: 10.1016/j.epsl.2009.12.035.

Liebke U, Appel E, Ding L, Neumann U, Antolin A, Xu Q. 2010. Position of the Lhasa terrane prior to India-Asia collision derived from palaeomagnetic inclinations of 53 Ma old dykes of the Linzhou Basin: Constraints on the age of collision and post-collisional shortening within the Tibetan Plateau. Geophysical Journal International, 182, 1199–1215. doi: 10.1111/j.1365-246X.2010.04698.x.

Liu XM, Yuan HL, Hattendorf B, Gunther D, Chen L, Hu SH. 2002. Analysis of 42 major and trace elements in glass standard reference materials by 193nm LA-ICPMS. Acta Petrologica Sinica, 18(3), 408–418 (in Chinese with English abstract).

Liu ZC, Wu FY, Ji WQ, Wang JG, Liu CZ. 2014. Petrogenesis of Ramba leucogranite in the Tethyan Himalaya and constraints on the channel flow model. Lithos, 208 –209, 118–136. doi: 10.1016/j.lithos.2014.08.022.

Miles AJ, Graham CM, Hawkesworth CJ, Gillespie MR, Hinton RW. 2013. Evidence for distinct stages of magma history recorded by the compositions of accessory apatite and zircon. Contributions to Mineralogy and Petrology, 166, 1–19. doi: 10.1007/s00410-013-0862-9.

Miles AJ, Graham CM, Hawkesworth CJ, Gillespie MR, Hinton RW, Bromiey GD, Mac EM. 2014. Mn in apatite: A new redox proxy for silicic magmas? Geochimica et Cosmochimica Acta, 132, 101–119. doi: 10.1016/j.gca.2014.01.040.

Montel JM. 1993. A model for monazite/melt equilibrium and the application to the generation of granitic magmas. Chemical Geology, 110, 127–46. doi: 10.1016/0009-2541(93)90250-M.

Morton A, Yaxley G. 2007. Detrital apatite geochemistry and its application in provenance studies. Special Paper of the Geological Society of America, 420, 319–344. doi: 10.1130/2006.2420(19).

Murphy MA, Harrison TM. 1999. Relationship between leucogranites and the Qomolangma detachment in the Rongbuk Valley, south Tibet. Geology, 27(9), 831–834. doi: 10.1130/0091-7613(1999)027<0831:RBLATQ>2.3.CO;2.

Pan LC, Hu, RZ, Wang XS, Bi XW, Zhu JJ, Li C. 2016. Apatite trace element and halogen compositions as petrogenetic-metallogenic indicators: Examples from four granite plutons in the sanjiang region,SWChina.Lithos,254-255,118–130.doi:10.1016/j.lithos.2016.03.010.

Patrick B, Bell EA, Thomas S, Reto T, Brenhin KC, Pardo OS, Davis AM, Harrison TM, Pellin MJ. 2018. Potassic, high-silica hadean crust. Proceedings of the National Academy of Sciences, 115, 6353. doi: 10.1073/pnas.1720880115.

Pearce NJG, Perkins WT, Wetgate JA, Gorton MP, Jackson SE, Neal CR, Chenery P. 1997. A compilation of new and published major and trace element data for NIST SRM610 and NIST SRM 612 glass reference materials. Geostandards Newsletters, 21, 115–144. doi: 10.1111/j.1751-908X.1997.tb00538.x.

Piccoli PM, Candela PA. 2002. Apatite in igneous systems. Reviews in Mineralogy and Geochemistry, 48, 255–292. doi: 10.2138/rmg.2002.48.6.

Pichavant M, Montel JM, Richard LR. 1992. Apatite solubility in peraluminous liquids: Experimental data and an extension of the Harrison-Watson model. Geochimica et Cosmochimica Acta, 56, 3855–3861. doi: 10.1016/0016-7037(92)90178-L.

Rapp RP, Watson EB. 1986. Monazite solubility and dissolution kinetics: Implications for the thorium and light rare earth chemistry of felsic magmas. Contributions to Mineralogy and Petrology, 94, 304–316. doi: 10.1007/BF00371439.

Searle MP, Godin L. 2003. The south Tibetan detachment and the Manaslu Leucogranite: A structural reinterpretation and restoration of the Annapurna-Manaslu Himalaya, Nepal. The Journal of geology, 111(5), 505–523. doi: 10.1086/376763.

Streule M, Searle M, Waters D, Horstwood M. 2010. Metamorphism, melting, and channel flow in the Greater Himalayan Sequence and Makalu leucogranite: Constraints from thermobarometry, metamorphic modeling, and U-Pb geochronology. Tectonics, 29(5), TC5011. doi: 10.1029/2009TC002533.

Sun SS, McDonough WF. 1989. Chemical and isotopic systematics of oceanic basalts: Implications for mantle composition and processes. Geological Society, London, Special Publications, 42, 313–345. doi: 10.1144/GSL.SP.1989.042.01.19.

Villaros A, Stevens, G, Moyen J, Buick IS. 2009. The trace element compositions of S-type granites: Evidence for disequilibrium melting and accessory phase entrainment in the source. Contributions to Mineralogy and Petrology, 158, 543–561. doi: 10.1007/s00410-009-0396-3.

Watson EB, Harrison TM. 1984. Accessory minerals and the geochemical evolution of crustal magmatic system: A summary and prospectus of experimental approaches. Physics of the Earth and Planetary Interiors, 35, 19–30. doi: 10.1016/0031-9201(84)90031-1.

Wolf MB, London D. 1995. Incongruent dissolution of REE- and Sr-rich apatite in peraluminous granitic liquids: Differential apatite, monazite and xenotime solubilities during anatexis. American Mineralogist, 80(7–8), 765–775. doi: 10.2138/am-1995-7-818.

Yang XY, Zhang JJ, Qi GW. 2009. Structure and deformation around the Gyirong basin, northern Himalaya, and onset of the south Tibetan detachment system. Science in China Series D: Earth Sciences, 52, 1046–1058. doi: 10.1007/s11430-009-0111-2.

Yin A, Harrison TM. 2000. Geologic evolution of the Himalayan-Tibetan orogen. Annual Review of Earth and Planetary Sciences, 28, 211–280. doi: 10.1146/annurev.earth.28.1.211.

Yu JJ, Zeng LS, Liu J, Gao LE, Xie KJ. 2011. Early Miocene leucogranites in Dinggye area, southern Tibet: Formation mechanism and tectonic implications. Acta Petrologia Sinica, 27(7), 1961–1972 (in Chinese with English abstract).

Zeng LS, Asimow PD, Saleeby JB. 2005b. Coupling of anatectic reactions and dissolution of accessory phases and the Sr and Nd isotope systematics of anatectic melts from a metasedimentary source. Geochimica et Cosmochimica Acta, 69(14), 3671–3682. doi: 10.1016/j.gca.2005.02.035.

Zeng LS, Gao LE, Xie KJ, Liu J. 2011. Mid-Eocene high Sr/Y granites in the Northern Himalayan gneiss domes: Melting thickened lower continental crust. Earth and Planetary Science Letters, 303, 251–266. doi: 10.1016/j.epsl.2011.01.005.

Zeng LS, Saleeby JB, Asimow P. 2005a. Nd isotope disequilibrium during crustal anatexis: A record from the Goat Ranch migmatite complex, southern Sierra Nevada batholith, California. Geology, 33, 53–56. doi: 10.1130/G20831.1.

Zeng LS, Chen J, Gao LE, Chen ZY. 2012. The geochemical nature of apatites in high Sr/Y two-mica granites from the North Himalayan Gneiss Domes, southern Tibet. Acta Petrologica Sinica, 28(9), 2981–2993 (in Chinese with English abstract).

Zeng LS, Gao LE. 2017. Cenozoic crustal anatexis and the leucogranites in the Himalayan collisional orogenic belt. Acta Petrologica Sinica, 33(5), 1420–1444 (in Chinese with English abstract).

Zhang HF, Harris N, Parrish R, Kelley S, Zhang L, Rogers N, Argles T, King J. 2004. Causes and consequences of protracted melting of the mid-crust exposed in the North Himalayan antiform. Earth and Planetary Science Letters, 228, 195–212. doi: 10.1016/j.epsl.2004.09.031.